Research Article Vol. 34, No. 5 / 9 Mar 2026 / Optics Express 7758

Optics EXPRESS

Highly efficient thermo-optic phase shifters for UV photonic applications

HAN WANG,[1,2] TEREZA BACOVA,[1,3] ANABEL DE PROFT,[1] MICHIEL DEBAETS,[1] NGA PHAM,[1] POL VAN DORPE,[1,2] CHRISTIAN HAFFNER,[1] AND PIETER NEUTENS[1,*]

[1] *Imec, Kapeldreef 75, 3001 Leuven, Belgium*
[2] *Department of Physics and Astronomy, KU Leuven, Celestijnenlaan 200D, B-3001 Leuven, Belgium*
[3] *Faculty of Mechanical Engineering (FME), Brno University of Technology, Technická 2896, 616 69 Brno, Czech Republic*
[*] *Pieter.Neutens@imec.be*

Abstract: We propose highly efficient, thermo-optic phase shifters based on aluminum oxide waveguides operating at UV wavelengths. The phase shifters are integrated into Mach-Zehnder interferometers for device characterization. The photonic waveguides are fabricated in a 200 mm CMOS pilot line, and heaters and silicon undercut are defined on the die-level with metal lift-off and dry etching processes. We experimentally demonstrate a phase shifter with an efficiency of 0.85 mW for a π phase shift at 360 nm wavelength. For the bandwidth characterization, we measure the 10 – 90% rise and fall times of a series of phase shifters with varying structural designs and systematically analyze the trade-off between efficiency and response time. The developed device provides a low insertion loss, high-efficiency active modulator that can be readily integrated onto the existing 200 mm aluminum oxide UV photonics platform.

1. Introduction

Ultraviolet (UV) light has attracted significant interest in fields such as spectroscopy [1], life sciences [2] and quantum optics [3], due to its high photon energy, which enables efficient excitation of molecular transitions. In recent years, significant advancements have been made in the domain of integrated photonics, particularly for systems operating within the near-infrared and visible spectral regions, ranging from the reduced optical propagation loss [4–6] and hybrid or heterogeneous integration of active components [7–10] to the demonstration of complex photonic integrated circuits (PICs) for practical applications [11–17]. However, it remains a major challenge to extend the working range of integrated photonics into the UV regime. This is primarily because silicon (Si) and silicon nitride (SiN), currently the most commonly used material platforms, are not transparent in the UV range, as their relatively narrow bandgaps result in significant material absorption at such short wavelengths. The emerging alternative wide-bandgap material platforms for UV photonics are aluminum oxide (Al_2O_3) [18,19] and aluminum nitride (AlN) [20], both offering optical transparency in the UV spectrum and complementary metal-oxide semiconductor (CMOS) compatibility. Compared with AlN, which suffers from the relatively high waveguide propagation loss, Al_2O_3 provides a promising platform combining the low optical propagation loss at UV wavelengths with full CMOS compatibility. To date, the Al_2O_3 platform has been fabricated using a 200 mm CMOS pilot line [18] and demonstrated in several applications such as Raman spectroscopy [21], optical imaging [22,23] and addressing of trapped ions in quantum computing applications [3].

Despite the notable progress achieved in passive devices for Al_2O_3 integrated photonics, the absence of active components continues to hinder its further development. For example, integrated lasers [7–9] and detectors [10] can autonomously generate and receive the light propagating in the waveguides, eliminating the requirement for external fiber coupling and enabling PICs to operate

#582592 https://doi.org/10.1364/OE.582592
Journal © 2026 Received 24 Oct 2025; revised 14 Jan 2026; accepted 14 Jan 2026; published 25 Feb 2026

independently. On-chip modulators [24] can further enhance the flexibility and reconfigurability of PICs by dynamically tuning optical properties such as wavelength, intensity, phase, and polarization. The thermo-optic phase shifter [25–27] is a basic phase modulator that is used widespread for various applications including optical phased arrays [13], programmable photonic circuits [28] and optical neural networks [15,29]. Owing to the thermo-optic effect, the optical phase can be finely controlled via locally heating the waveguide to induce refractive index change. Unlike the electro-optic phase shifters that leverage the Pockels effect, thermo-optic phase shifters can be implemented in centrosymmetric materials such as SiN and Al_2O_3 without second-order nonlinearity. However, the waveguide is thermally shorted to the bulk Si substrate through the silicon oxide (SiO_2) cladding, and the heat spreads into the substrate by this low-thermal-resistance path, leading to higher power consumption for phase shift. In addition, Al_2O_3 exhibits a relatively low thermo-optic coefficient, further increasing power consumption. Such thermo-optic phase shifters with high power consumption pose a major challenge for the future deployment of UV PICs.

Here, we present highly efficient Al_2O_3 thermo-optic phase shifters for UV wavelengths. By leveraging the silicon substrate undercut etching to construct a suspended waveguide structure, we dramatically reduce P_π, the driving power of heater required to generate a π phase shift, from 49 mW to 0.85 mW. Similar suspended heater structures have been demonstrated at near-infrared spectrum in Si waveguides [30–32] and SiN waveguides [33,34], at visible spectrum in SiN waveguides [35–39], and also at mid-infrared spectrum in indium gallium arsenide (InGaAs) waveguides [40]. To the best of our knowledge, this work is the first demonstration of such an efficient phase shifter in the UV range. As a mature technique in CMOS-compatible pilot lines, the suspended structures have already been demonstrated on the wafer-scale Si and SiN PICs [32,35,38]. As all used processes are CMOS compatible, it can also be readily adopted on the imec 200 mm pilot line to realize a fully integrated UV photonic platform in conjunction with low-loss passive waveguides [18] and edge couplers [41] that we previously developed, which will pave the way toward chip-scale applications in biomedical sensing and quantum computing at UV wavelengths.

2. Design and simulations

The thermo-optic phase shifters are designed on the Al_2O_3-based UV photonics platform previously developed by our group [18]. The alumina waveguide thickness is 110 nm, and the single-mode width is 450 nm for operation at 360 nm wavelength. The typical single-mode waveguide propagation loss is 0.60 ± 0.17 dB/cm, measured over all dies on a 200 mm wafer. Since the phase shift cannot be measured directly, each phase shifter is incorporated into one arm of an unbalanced Mach-Zehnder interferometer (MZI) with an arm length difference of 5 μm, enabling calculation of the phase shift from the measured optical power transmission. The schematic layout is shown in Fig. 1(a). Each MZI consists of the 1×2 and 2×2 multimode interference couplers with insertion losses of 0.014 and 0.074 dB, respectively, yielding the MZI insertion loss of 0.18 dB. The cross-sectional schematic of the phase shifter with indication of the device dimensions is displayed in Fig. 1(c3). The tungsten (W) heater with a width of 3 μm and a thickness of 100 nm is placed 1.06 μm above the waveguide. To form the suspended beam, a pair of 15 μm wide trenches with 10 μm separation are added and centered around the waveguide by removing the surrounding SiO_2, and an undercut on the bottom is created by removing a part of Si substrate.

For thermal modeling and analysis, COMSOL Multiphysics was used to simulate the thermo-optic phase shifter performance. To assess the impact of structural configurations, three phase shifters with different cross-sectional geometries were simulated and compared: (i) without the trench and the undercut (Fig. 1(c1)), (ii) with only the trench (Fig. 1(c2)), and (iii) with both the trench and an undercut (Fig. 1(c3)). In the thermal simulation, the applied power for the W heater

Optics EXPRESS

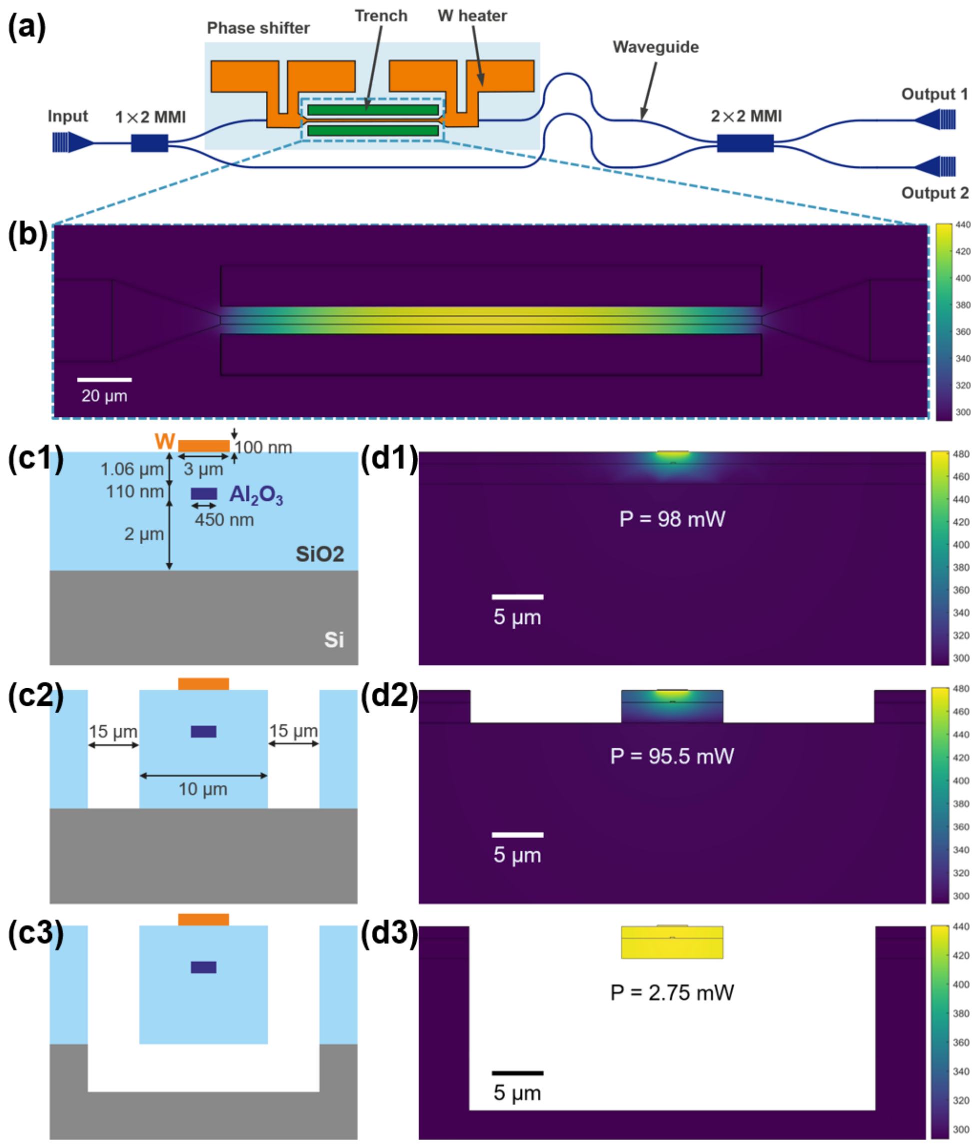

Fig. 1. Thermo-optic phase shifter design. (a) Schematic layout of a MZI integrated with a phase shifter (not to scale). (b) Thermal simulation of the phase shifter with the suspended structure driven at 2.75 mW of power. (c1-c3) Cross-sectional schematics of the phase shifters without trench and undercut, with only trench and with both trench and undercut. (d1-d3) Corresponding simulated cross-section temperature distribution profiles at 98, 95.5 and 2.75 mW, respectively.

are 98 mW and 95.5 mW in structures (i) and (ii), respectively, whereas structure (iii) requires only 2.75 mW. According to the corresponding simulated temperature distribution profiles presented in Fig. 1(d1-d3), the waveguide temperature can reach 440 K with the temperature difference of 1 K between the heater and waveguide in configuration (iii), while the waveguide temperature is only 406 K with the temperature difference of 80 K in (i) and (ii). The simulation results clearly indicate that, in contrast to configurations (i) and (ii), the introduction of an undercut shown in

Optics EXPRESS

(iii) substantially improves the thermal insulation by effectively localizing heat within the core region.

The MZI phase shift $\Delta\varphi$ is expressed as:

$$\Delta\varphi = \frac{2\pi L}{\lambda}\frac{dn_{\text{eff}}}{dT}\Delta T, \tag{1}$$

where L is the waveguide length below the heater, λ=360 nm is the wavelength, n_{eff} is the effective index, $\text{d}n_{\text{eff}}/\text{d}T$ is the thermo-optic coefficient of Al_2O_3, and ΔT is the temperature change. In order to investigate the influence of different geometric parameters, the P_π of each phase shifter is extracted from simulation results, shown in Fig. 2, where measurement results detailed in section 4.1 are also summarized to validate the simulations.

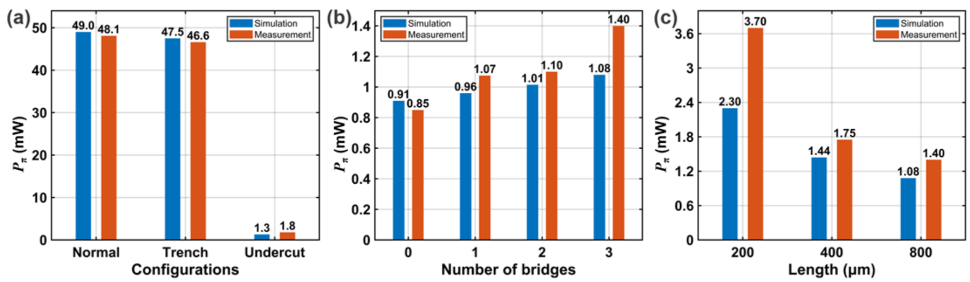

Fig. 2. The simulated and measured P_π of the thermo-optic phase shifters with varying structural designs. (a) Comparison of phase shifters ($L = 400\,\mu$m, 2 bridges) without and with the undercut structure, showing a reduction of P_π from ~49 mW to ~1.3 mW leveraging the undercut. (b) Comparison of 800 µm long phase shifters with varying numbers of bridges supporting suspended region. (c) Comparison of phase shifters with 3 bridges for varying device lengths.

Figure 2(a) shows the simulated power consumption of the thermo-optic phase shifters with $L = 200\,\mu$m but different structural configurations. The phase shifter without trench or undercut requires a P_π of 49.0 mW and the phase shifter with only trench demands P_π of 47.5 mW. By comparison, the undercut structure dramatically reduces the value to 1.3 mW. In to Fig. 2(b), the influence of the number of supporting bridges on P_π is investigated. The bridges increase the effective stiffness and buckling load of the suspended beam, thereby enhancing mechanical stability, mitigating the risk of fracture, and extending the device life time. However, bridges also provide a thermal leakage path to the Si substrate and thus increase p_π. For the undercuts with the same length of 800 µm, calculated P_π values of 0.91, 0.96, 1.01 and 1.08 mW are demonstrated respectively from the phase shifters containing 0, 1, 2 and 3 bridges. Figure 2(c) studies the effect of the distinct undercut length. The simulated results shows that the phase shifters supported by three bridges with the 200, 400 and 800 µm long undercut necessitates a P_π of 2.30, 1.44 and 1.08 mW, respectively. The computational results demonstrate that, while an increased undercut length and a reduced number of bridge structures can compromise mechanical integrity, they contribute to improved phase shifter efficiency characteristics. This underscores a fundamental trade-off between structural robustness and efficiency.

3. Device fabrication

The integration process of the Al_2O_3 photonic waveguide embedded in a SiO_2 cladding was carried out in the imec 200 mm CMOS pilot line. The bottom cladding consists of 2 µm thermal SiO_2 film, the waveguide is patterned in a 110 nm thick Al_2O_3 layer deposited by atomic layer deposition and the top cladding is a 1.06 µm thick high-density plasma SiO_2 layer. The fabrication

Optics EXPRESS

process, photonics waveguide design and optical losses for UV and visible wavelengths on this low-loss, 200 mm wafer scale process, UV-compatible photonics platform have been reported in [18].

In this work, we diced a fully processed 200 mm photonics wafer, and subsequently developed the heater, SiO_2 trench and Si undercut modules on the die-level in the imec Xplore lab. A schematic of the process flow is displayed in Fig. 3(a), where the left column represents the cross-sectional structures, and the right column shows the corresponding the top views. In step (1), the heater pattern was defined by an optical lithography step with a Karl Suss MA6 mask aligner and a bilayer photoresist stack of LOR1A/IX845G. Then the 100 nm thick W film was deposited by sputtering, followed by lift-off in Microstrip 2001 to complete the W heater module. For the definition of the SiO_2 trench and the Si undercut, the same photoresist mask was used. The trench pattern was defined in step (2) by optical lithography again and a 9.8 µm thick triple layer photoresist of IX845G. In the subsequent fabrication step (3) and (4), the pattern on the photoresist layer was transferred to the 3.17 µm thick SiO_2 layer using a CHF_3/CF_4 based reactive ion etching (RIE) process. The undercut in the Si substrate was realized via a SF_6 based inductively coupled plasma reactive ion etching (ICP-RIE) process. Finally, an oxygen plasma etch was performed to remove the top surface of burned photoresist, the remaining photoresist was then removed in Microstrip 2001, followed by rinsing in a sequence of isopropyl alcohol and 1-propanol to ensure clean drying of the suspended structures.

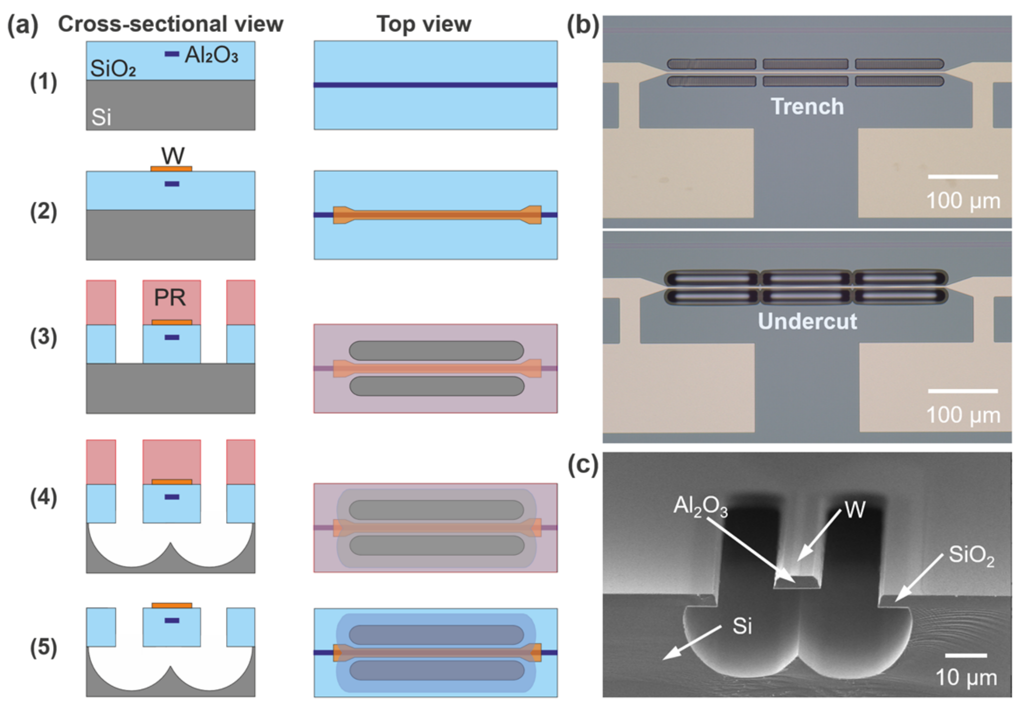

Fig. 3. Thermo-optic phase shifter fabrication. (a) Schematic process flow of the heater and undercut modules. Left: cross-sectional view. Right: top view. (1) Al_2O_3 PICs with patterned waveguides, (2) heater definition by lift-off process, (3) trench definition by lithography and SiO_2 etch, (4) undercut definition by Si isotropic etch, and (5) resist strip. (b) Top view microscope images of a 400 um long heater with SiO_2 trench and Si undercut with 2 tethers. (c) XSEM picture of the silicon undercut region.

The top view microscope images of MZIs with a 400 µm long and 3 µm wide heater, combined with only trenches and a Si undercut are shown in Fig. 3(b), and a cross-sectional scanning electron microscopy (XSEM) image of the undercut device is presented in Fig. 3(c), clearly displaying the suspended beam and isotropic Si etch. An upward deflection of the suspended beam caused by residual stress is observed. This issue will be mitigated in the next iteration by carefully selecting cladding and waveguide layers with opposing tensile and compressive stress to reduce the total stress in the suspended beam design.

4. Experimental results

4.1. Phase shifter efficiency

The opto-electrical measurement setup illustrated in Fig. 4(a) was built to characterize the phase tuning efficiency. The UV light from a continuous-wave (CW) laser operating at 360 nm is delivered in a single-mode fiber and coupled to the PIC via an input grating coupler. Its polarization is adjusted by a fiber polarization controller (not shown in the setup schematic). Active alignment of a single mode fiber to the output grating couplers of the MZI is performed to characterize the MZI transmission. The fiber-coupled optical power is quantified by a silicon photodetector and power meter. Electrically, the W heater is connected by a 4-needle DC probe in a 4-point measurement configuration, where the driving current for the heaters is supplied by a Keithley 2400 source meter unit while the voltage is measured on the sensing pads to accurately measure the power consumption by the integrated W heater.

The thermo-optic phase shifters are embedded in one arm of the MZIs, enabling the extraction of the phase shift from the optical power transmission. For each device, the heater power is swept while recording the MZI optical output power, allowing to calculate the power required to generate a π phase shift, P_{π}. To exclude the loss contribution from the grating couplers, the measurement is normalized to the power of a short reference waveguide with identical couplers. Figure 4(b-d) displays the MZI response as a function of the applied heater power for different device configurations. The peak value corresponds to the insertion loss (IL), the difference in minimum and maximum power represents the extinction ratio (ER), and half of the period is the metric for P_{π}.

In a first experiments, shown in Fig. 4(b), we compare the measured P_{π} of the same thermo-optic phase shifter with different trench and undercut configurations. The phase shifter is 800 um long heater without any bridges The conventional design without trench or undercut requires a power of 48.7 mW to drive a π phase shift. After introducing a deep trench, P_{π} slightly reduces to 47.4 mW, showing limited improvement. In contrast, fabricating the same device with silicon undercut achieves a substantially lower P_{π} of 0.85 mW, clearly demonstrating the efficiency enhancement enabled by our design. It is worth noting that all three phase shifters with distinct structures demonstrate similar insertion loss and extinction ratio, indicating that the undercut structure fabrication does not generate any degradation to the optical performance.

Next, we study the efficiency performance influenced by the number of supporting bridges in Fig. 4(c). For the undercuts with the same length of 800 µm, the phase shifters with 0, 1, 2, and 3 bridges exhibit P_{π} values of 0.85, 1.08, 1.1, and 1.4 mW, respectively. Adding more bridges improves mechanical stability, at the cost of marginally increasing power consumption.

Lastly, we investigate how the length of the undercut structure affects the device efficiency leveraging devices supported by three bridges. From the Fig. 4(d), a phase shifter with the 100 µm long undercut still necessitates P_{π} of 16.4 mW, which drops sharply to 3.7 mW by increasing the undercut length to 200 µm. Further extending the undercut length to 300, 400 and 800 µm reduces P_{π} to 2.35, 1.75 and 1.4 mW, respectively. These results indicate that longer undercut enhances thermal isolation and remarkably reduce the driving power requirement.

Optics EXPRESS

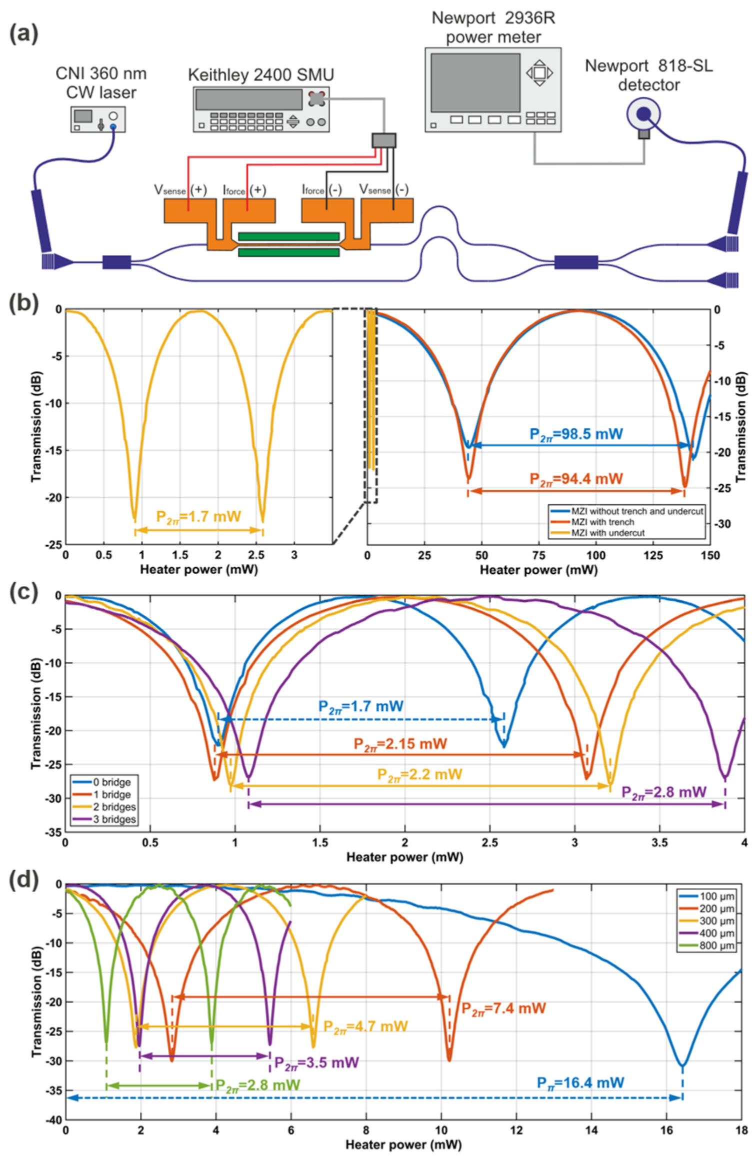

Fig. 4. Power efficiency characterization for thermo-optic phase shifters. (a) Schematic of the measurement setup. Blue: optical circuit. Gray: electrical circuit. (b-d) Measured optical transmission as a function of heater power. (b) Comparison of phase shifters ($L = 800\,\mu$m, no bridges) without and with undercut structure. The undercut reduces P_π from ~49 mW (no trench or with trench) to ~0.75 mW, confirming the significant efficiency improvement. (c) Comparison of 800 μm long phase shifters with varying numbers of bridges supporting suspended region. (d) Comparison of phase shifters with 3 bridges with varying lengths.

4.2. Phase shifter bandwidth

Although the thermal isolation of the heater area can drastically reduce the $P\pi$ required to achieve a π phase shift, it also causes a penalty in the temporal response of the thermo-optic phase shifter. By fabricating the undercut, the thermal conductance from the heater volume to the thermal ground decreases significantly. As the thermal time constant is inversely proportional to the

Optics EXPRESS

thermal conductance, the undercut will increase the thermal time constant and hence give rise to a slower phase shifter temporal response. Consequently, to design a thermo-optic phase shifter, one must find a compromise between efficiency and temporal response.

The time response of the thermo-optic phase shifters was characterized by the measurement setup schematically shown in Fig. 5(a), similar to that used in Section 4.1. In the optical measurement setup, the output fiber is connected to a Hamamatsu C5460-01 silicon avalanche photodiode (APD) with a 100 kHz frequency bandwidth. For the electrical driving circuit, a HP 8110A pulse generator is used to apply a square current pulse with the minimum and maximum current values set to modulate the phase shifter over the first full π phase shift. A 1 ms square pulse is applied with a period of 5 ms. The pulse generator output and APD output are connected to the high-impedance inputs of channels A and B of a Tektronix MSO 3014 oscilloscope to visualize the voltage across the heater and the phase shifter optical response. An 8× average is set for both time traces and the waveforms are saved to a data file for further data analysis.

Figure 5(b) displays the temporal response of a 400 µm long thermo-optic phase shifter with three different configurations: (1) without any SiO_2 trench or Si undercut, (2) with only the SiO_2 trench, and (3) with both the SiO_2 trench and a Si undercut supported by three tethers. For the device without trench or undercut, the measured 10% - 90% rise and fall times are 3.6 and 6.8 µs, respectively, which are close to the detector bandwidth-limited rise and fall times of ~3.5 µs. Therefore, we estimate its frequency bandwidth to exceed 68 kHz. For the device with only the SiO_2 trench, the observed rise and fall times of 3.1 and 7.5 µs corresponds to a minimum frequency bandwidth of ~66 kHz. The zoom-in results of the rise and fall time for these two phase shifters are shown in Fig. 5(c). In contrast, the device with both the SiO_2 trench and the Si undercut exhibits significantly slower dynamics, with recorded rise and fall times of 378.0 and 451.2 µs, corresponding to a device bandwidth of 0.85 kHz. This clearly demonstrates that introducing thermal isolation of the heater volume by the Si undercut can drastically improve the phase shifter efficiency, reducing the power consumption from 48.55 to 1.75 mW/π, but with the penalty of a dropped frequency bandwidth from >68 kHz down to 0.85 kHz. The obtained results are summarized in Table 1.

Table 1. Measurement result of phase shifters with different configurations

Device	Trench	Undercut	P_π (mW)	Rise (µs)	Fall (µs)	Bandwidth (kHz)
1	No	No	48.5	3.6	6.6	> 68.6
2	Yes	No	46.4	3.1	7.5	> 66.0
3	Yes	Yes	1.75	378.0	451.2	0.85

In Fig. 5(d), we study the dependence of the heater length for the bandwidth performance of thermo-optic phase shifter with three bridges. As the length increases from 100 µm to 400 µm, p_π decreases gradually from 16.4 mW to 1.75 mW, indicating an improve phase shifter efficiency. However, this comes at the cost of slower temporal response with the increasing rise and fall times, which leads to a reduction in modulation bandwidth from 7.0 kHz down to <1 kHz. The extracted results are listed in Table 2. The optimal configuration will be ultimately determined by the target application, and strongly depend on the available power budget, mechanical stability and required operational bandwidth.

In Fig. 6, we compare the performance of state-of-the-art thermo-optic phase shifters based on the suspended structure operating at sub-micron wavelengths. Our work achieves a low P_π of 0.85 mW at the UV wavelength of 360 nm, comparable to state-of-the-art values at visible wavelengths.

Optics EXPRESS

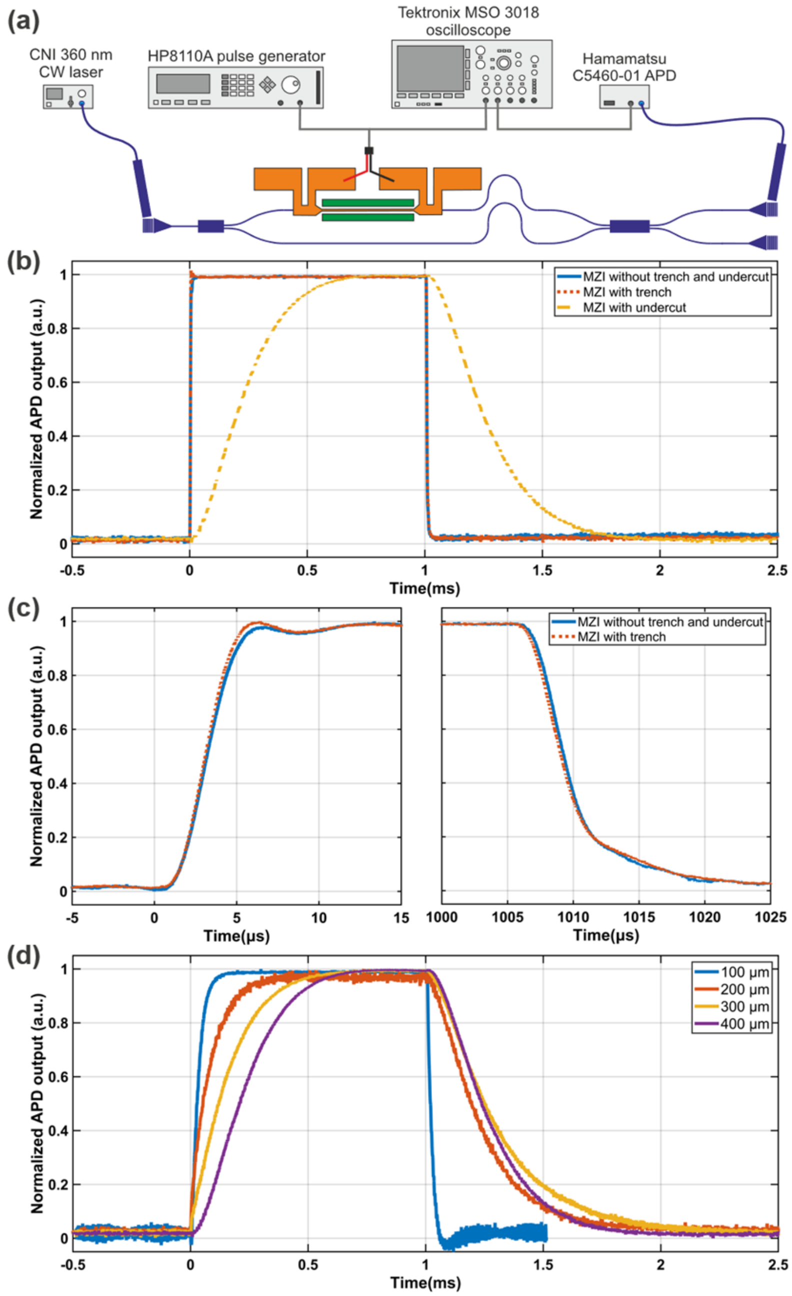

Fig. 5. Bandwidth characterization for thermo-optic phase shifters. (a) Schematic of the measurement setup. Blue: optical part. Gray: electrical part. (b-d) Measured time-domain response for a 1 ms square pulse. (b) Measured temporal responses of MZIs without trench or undercut (blue solid line), with only trench (red dotted line), and with both trench and undercut (yellow dashed line). (c) Zoom-in images of the rise and fall responses for the MZIs with trench or undercut (blue solid line), and with only trench (red dotted line). (d) Measured temporal responses of MZIs with undercuts at varying lengths.

Table 2. Measurement result of phase shifters with varying undercut lengths

Device	Length (μm)	P_π (mW)	Rise (μs)	Fall (μs)	Bandwidth (kHz)
1	100	16.4	64.8	35.0	7.0
2	200	3.7	210.4	432.4	1.1
3	300	2.35	329.6	590.8	0.76
4	400	1.75	378.0	451.2	0.84

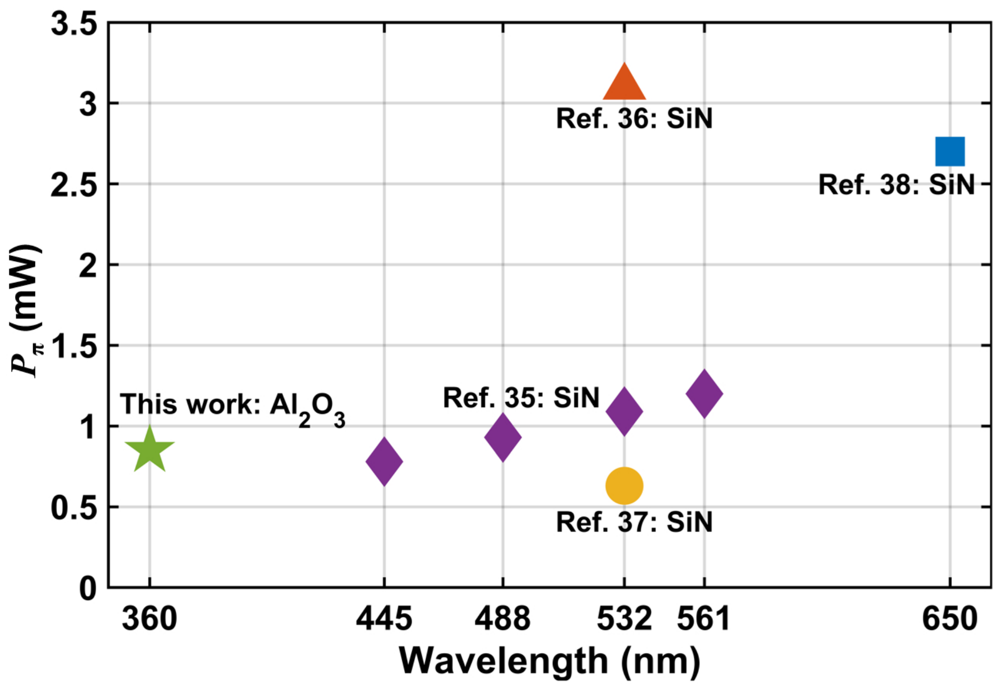

Fig. 6. Performance of the thermo-optic phase shifters leveraging the undercut for the sub-micron spectral range.

5. Discussion and conclusion

In summary, we propose a highly efficient Al_2O_3 UV thermo-optic phase shifter. The devices are fabricated by the combination of the wafer-scale processing and the die-level post-processing, and it is promised to be fully compatible with standard 200 mm CMOS pilot line. Owing to the introduction of the undercut structure, the low P_π of 0.85 mW at 360 nm wavelength is achieved because of the thermal insulation. The temporal bandwidth is also investigated, revealing a clear trade-off between power consumption and modulation speed. The power consumption can be further decreased by employing the densely folded waveguide design [31,35,42], and this device can also be extended to the micro-ring based filter [32,43]. In short, this work provides a straightforward solution to realize on-chip modulator in the UV photonics platform, which has strong potential to assist a wide range of UV applications for the life science and quantum information processing.

Acknowledgment. The authors thank Glen Maes for XSEM, Johan Feyaerts, Johan De Cooman, Kim Baumans, Patrick Verdonck and Myriam Willegems for help in the cleanroom, Philippe Helin and Gaudhaman Jeevanandam for 200 mm process integration and Zeinab Jafari, Erfan Mafakheri and Roelof Jansen for assistance with photonics design.

Optics EXPRESS

Disclosures. The authors declare no conflicts of interest.

Data availability. Data underlying the results presented in this paper are not publicly available at this time but may be obtained from the authors upon reasonable request.

References

1. V. Schuster, C. Liu, R. Klas, *et al.*, "Ultraviolet dual comb spectroscopy: a roadmap," Opt. Express **29**(14), 21859–21875 (2021).
2. S. A. Oladepo, K. Xiong, Z. Hong, *et al.*, "UV resonance Raman investigations of peptide and protein structure and dynamics," Chem. Rev. **112**(5), 2604–2628 (2012).
3. J. Kwon, W. J. Setzer, M. Gehl, *et al.*, "Multi-site integrated optical addressing of trapped ions," Nat. Commun. **15**(1), 3709 (2024).
4. A. Z. Subramanian, P. Neutens, A. Dhakal, *et al.*, "Low-loss singlemode PECVD silicon nitride photonic wire waveguides for 532–900 nm wavelength window fabricated within a CMOS pilot line," IEEE Photonics J. **5**(6), 2202809 (2013).
5. W. D. Sacher, X. Luo, Y. Yang, *et al.*, "Visible-light silicon nitride waveguide devices and implantable neurophotonic probes on thinned 200 mm silicon wafers," Opt. Express **27**(26), 37400–37418 (2019).
6. X. Ji, R. N. Wang, Y. Liu, *et al.*, "Efficient mass manufacturing of high-density, ultra-low-loss Si_3N_4 photonic integrated circuits," Optica **11**(10), 1397–1407 (2024).
7. A. Marinins, S. Hansch, H. Sar, *et al.*, "Wafer-scale hybrid integration of InP DFB lasers on Si photonics by flip-chip bonding with sub-300 nm alignment precision," IEEE J. Select. Topics Quantum Electron. **29**(3), 1–11 (2022).
8. X. Mu, F. Weiss, H. Chua, *et al.*, "Flip-chip bonded 450-nm InGaN laser diodes in a foundry fabricated visible-light silicon photonics platform," in *Optical Fiber Communication Conference (OFC) 2025 (2025), Paper M1 K.5* (Optica Publishing Group, 2025), p. M1 K.5.
9. M. Kiewiet, S. Cuyvers, M. Billet, *et al.*, "Micro-transfer printed continuous-wave and mode-locked laser integration at 800 nm on a silicon nitride platform," Laser Photonics Rev e00956 (2025).
10. S. Cuyvers, A. Hermans, M. Kiewiet, *et al.*, "Heterogeneous integration of Si photodiodes on silicon nitride for near-visible light detection," Opt. Lett. **47**(4), 937–940 (2022).
11. P. Neutens, J. O'Callaghan, J. De Ceulaer, *et al.*, "Dual-wavelength neural probe for simultaneous opto-stimulation and recording fabricated in a monolithically integrated CMOS/photonics technology platform," in *2023 International Electron Devices Meeting (IEDM)* (2023), pp. 1–4.
12. S. Jooken, K. Zinoviev, G. Yurtsever, *et al.*, "On-chip flow cytometer using integrated photonics for the detection of human leukocytes," Sci. Rep. **14**(1), 10921 (2024).
13. F. Milojković, N. Verellen, R. Jansen, *et al.*, "Focusing through scattering media using integrated photonics," ACS Photonics **11**(10), 4288–4296 (2024).
14. A. Lukashchuk, H. K. Yildirim, A. Bancora, *et al.*, "Photonic-electronic integrated circuit-based coherent LiDAR engine," Nat. Commun. **15**(1), 3134 (2024).
15. Y. Shen, N. C. Harris, S. Skirlo, *et al.*, "Deep learning with coherent nanophotonic circuits," Nat. Photonics **11**(7), 441–446 (2017).
16. S. Hua, E. Divita, S. Yu, *et al.*, "An integrated large-scale photonic accelerator with ultralow latency," Nature **640**(8058), 361–367 (2025).
17. S. R. Ahmed, R. Baghdadi, M. Bernadskiy, *et al.*, "Universal photonic artificial intelligence acceleration," Nature **640**(8058), 368–374 (2025).
18. P. Neutens, E. Mafakheri, X. Zheng, *et al.*, "A 200 mm wafer-scale Al2O3 photonics waveguide technology for UV and visible applications," IEEE Photonics J. **17**(3), 1–6 (2025).
19. T. Gök, R. Thomas, A. Sorokina, *et al.*, "Evaporated aluminum oxide (Al_2O_3) single-mode waveguides with less than 0.7 dB/cm propagation loss at 405 nm," Opt. Mater. Express **15**(8), 1966–1971 (2025).
20. T.-J. Lu, M. Fanto, H. Choi, *et al.*, "Aluminum nitride integrated photonics platform for the ultraviolet to visible spectrum," Opt. Express **26**(9), 11147–11160 (2018).
21. A. Raza, S. Clemmen, P. Wuytens, *et al.*, "High index contrast photonic platforms for on-chip Raman spectroscopy," Opt. Express **27**(16), 23067–23079 (2019).
22. C. Lin, J. S. D. Peñaranda, J. Dendooven, *et al.*, "UV photonic integrated circuits for far-field structured illumination autofluorescence microscopy," Nat. Commun. **13**(1), 4360 (2022).
23. C. Lin, Y. Guo, and N. L. Thomas, "Demonstration of a photonic integrated circuit for quantitative phase imaging," Photonics Res. **13**(1), 1–17 (2025).
24. A. Rahim, A. Hermans, B. Wohlfeil, *et al.*, "Taking silicon photonics modulators to a higher performance level: state-of-the-art and a review of new technologies," Adv. Photonics **3**(2), 024003 (2021).
25. S. Liu, J. Feng, Y. Tian, *et al.*, "Thermo-optic phase shifters based on silicon-on-insulator platform: state-of-the-art and a review," Front. Optoelectron. **15**(1), 9 (2022).
26. F. Gao, W. Xie, J. Y. S. Tan, *et al.*, "Comprehensive investigation of thermo-optic phase shifters on a multi-layered SiN-on-SOI platform," J. Lightwave Technol. **41**(10), 3108–3114 (2023).
27. J. Parra, J. Navarro-Arenas, and P. Sanchis, "Silicon thermo-optic phase shifters: a review of configurations and optimization strategies," Adv. Photon. Nexus **3**(4), 044001 (2024).
28. W. Bogaerts, D. Pérez, J. Capmany, *et al.*, "Programmable photonic circuits," Nature **586**(7828), 207–216 (2020).

Optics EXPRESS

29. T. Fu, J. Zhang, R. Sun, *et al.*, "Optical neural networks: progress and challenges," Light:Sci. Appl. **13**(1), 263 (2024).
30. R. Kasahara, K. Watanabe, M. Itoh, *et al.*, "Extremely low power consumption thermooptic switch (0.6 mW) with suspended ridge and silicon-silica hybrid waveguide structures," in *2008 34th European Conference on Optical Communication*, 1–2 (2008).
31. Z. Lu, K. Murray, H. Jayatilleka, *et al.*, "Michelson interferometer thermo-optic switch on SOI with a 50-μW power consumption," IEEE Photon. Technol. Lett. **27**(22), 2319–2322 (2015).
32. R. Parsons, K. Jang, Y. Wang, *et al.*, "Highly uniform thermally undercut silicon photonic devices in a 300 mm CMOS foundry process," Sci. Rep. **15**(1), 29906 (2025).
33. S. Lin, Y. Zhang, Z. Wu, *et al.*, "Power-efficient programmable integrated multiport photonic interferometer in CMOS-compatible silicon nitride," Photonics Res. **12**(3), A11–A20 (2024).
34. J. Zeng, J. Li, S. Lin, *et al.*, "Submilliwatt silicon nitride thermo-optic phase shifter enabled by a dense sinusoidal spiral waveguide," Opt. Lett. **50**(11), 3768–3771 (2025).
35. Z. Yong, H. Chen, X. Luo, *et al.*, "Power-efficient silicon nitride thermo-optic phase shifters for visible light," Opt. Express **30**(5), 7225–7237 (2022).
36. Z. Wu, Y. Zhang, S. Zeng, *et al.*, "Laser beam steering of 532 nm using a power-efficient focal plane array," Opt. Lett. **48**(24), 6400–6403 (2023).
37. Z. Wu, S. Lin, S. Yu, *et al.*, "Submilliwatt silicon nitride thermo-optic modulator operating at 532 nm," Photonics **11**(3), 213 (2024).
38. Y. Gebregforgis, V. S. Sundaram, G. Nelson, *et al.*, "Highly-efficient visible-wavelength compact silicon-nitride thermo-optic phase shifter using undercut TiN heater," in *2025 Conference on Lasers and Electro-Optics (CLEO)* (2025), pp. 1–2.
39. H. Chen, T. Xue, Z. Yong, *et al.*, "Thermally induced refractive index trimming of visible-light silicon nitride waveguides using suspended heaters," Opt. Express **33**(23), 48925–48944 (2025).
40. P.-Y. Hsiao, J. Midkiff, P. Camp, *et al.*, "Suspended mid-infrared guided-wave phase shifters in an InP-based platform," in *CLEO 2024 (2024)*, Paper JTh2A.101 (Optica Publishing Group, 2024), p. JTh2A.101.
41. C. Lin, M. Kiewiet, R. R. Petit, *et al.*, "Ultra-low loss and large bandwidth fiber-to-chip edge coupler for aluminum oxide photonic platform at UV-visible wavelengths," J. Lightwave Technol. **43**(15), 7265–7269 (2025).
42. K. Murray, Z. Lu, H. Jayatilleka, *et al.*, "Dense dissimilar waveguide routing for highly efficient thermo-optic switches on silicon," Opt. Express **23**(15), 19575–19585 (2015).
43. W. Bogaerts, P. De Heyn, T. Van Vaerenbergh, *et al.*, "Silicon microring resonators," Laser Photonics Rev. **6**(1), 47–73 (2012).